PHYSICAL REVIEW E **82**, 051923 (2010)

Comparison of Brownian-dynamics-based estimates of polymer tension with direct force measurements

Mark E. Arsenault,[1] Prashant K. Purohit,[1] Yale E. Goldman,[2] Henry Shuman,[2] and Haim H. Bau[1,*]
[1]*Department of Mechanical Engineering and Applied Mechanics, University of Pennsylvania, Towne Building, 220 S. 33rd St., Philadelphia, Pennsylvania 19104-6315, USA*
[2]*Pennsylvania Muscle Institute, School of Medicine, University of Pennsylvania, D-700, Richards Building, 3700 Hamilton Walk, Philadelphia, Pennsylvania 19104, USA*

(Received 15 June 2010; revised manuscript received 16 September 2010; published 17 November 2010)

With the aid of Brownian dynamics models, it is possible to estimate polymer tension by monitoring polymers' transverse thermal fluctuations. To assess the precision of the approach, Brownian dynamics-based tension estimates were compared with the force applied to rhodamine-phalloidin labeled actin filaments bound to polymer beads and suspended between two optical traps. The transverse thermal fluctuations of each filament were monitored with a CCD camera, and the images were analyzed to obtain the filament's transverse displacement variance as a function of position along the filament, the filament's tension, and the camera's exposure time. A linear Brownian dynamics model was used to estimate the filament's tension. The estimated force was compared and agreed within 30% (when the tension <0.1 pN) and 70% (when the tension <1 pN) with the applied trap force. In addition, the paper presents concise asymptotic expressions for the mechanical compliance of a system consisting of a filament attached tangentially to bead handles (dumbbell system). The techniques described here can be used for noncontact estimates of polymers' and fibers' tension.

DOI: 10.1103/PhysRevE.82.051923 PACS number(s): 87.80.Nj, 87.15.La, 87.16.Ka, 87.80.Fe

I. INTRODUCTION

When using electrostatic forces to position actin filaments across gaps between electrode pairs, Arsenault *et al.* [1,2] observed that the amplitude of the filaments' lateral vibrations decreased as the electric field's intensity increased. To estimate filament tension, Arsenault *et al.* [1] measured the variance of the filament's transverse thermal fluctuations, assumed that the filament behaves like a slender elastic beam, and used a simple Brownian-dynamics model and the principle of equipartition of energy to match the predicted and measured variances.

The use of Brownian dynamics models and the principle of equipartition of energy to estimate the mechanical properties of polymers is not new. Yanagida *et al.* [3] and Gittes *et al.* [4] deduced the flexural rigidities of freely diffusing actin filaments' and microtubules' from their modes of vibrations. Since the apparent tension of doubly anchored polymers has not been estimated before, we felt it prudent to verify the method by comparing the Brownian dynamics-based force estimates with direct force measurements.

Optical traps (laser tweezers) provide a convenient means to simultaneously apply forces in the range of piconewtons and measure subnanometer displacements. The optical trap was pioneered in the 1970s [5,6] and is commonly employed to study molecular motors [7–9] and cytoskeletal filaments and nucleic acids [10–14] at the single-molecule level. In these assays, micron-sized particles, trapped by tightly focused laser beams, act as handles to manipulate attached molecules of interest. The angular intensity distribution of the laser light as it enters and leaves the trap allows one to estimate the force acting on the bead [15]. When displacements are small, the trap acts like a linear spring.

Wang *et al.* [16] used optical tweezers to obtain similar results for the bending rigidity of DNA as those obtained with the application of hydrodynamic and magnetic forces to DNA filaments [17]. Optical tweezer studies of the shear moduli of filamentous networks [18] yielded similar results to earlier rheological techniques [19]. Here, we measure the variance of the transverse fluctuations of an actin filament anchored at each end to a bead held in an optical trap and subjected to tension. The measured variance is used to estimate the filament's tension, which is then compared with the applied force values.

II. MATERIALS AND METHODS

A 150-μm-high flow cell, confined between two glass coverslips was filled with a solution of 50 nM rhodamine-phalloidin-stabilized actin, polymerized in 2 mM $MgCl_2$, 150 mM KCl, and 2 mM Hepes (pH=7.4). The solution also included 1 mg/mL BSA to prevent nonspecific adhesion of the actin filaments to the glass surfaces and 50 mM DTT, 7.2 mg/mL glucose, 9 units/mL catalase, and 4 mg/mL glucose oxidase to slow rhodamine's photobleaching. Buffers were prepared with either 0% or 60% (by mass) glycerin to study the effect of the suspending medium's viscosity on the filaments' vibrations. The 0% and 60% glycerin buffers had, respectively, viscosities of 1 and 10.8 mPa s [20]. Subsequently, 1-μm-diameter, N-ethylmaleimide (NEM)-myosin-coated beads were infused into a flowcell. These beads were prepared as previously described [21]. The flowcell was sealed with grease to prevent solvent evaporation and was placed on the stage of an inverted microscope (Olympus IX70).

---

[*] Corresponding author; bau@seas.upenn.edu

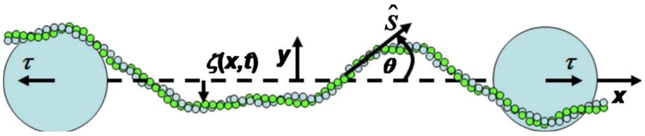

FIG. 1. (Color online) A schematic depiction of the experimental setup and the coordinate system. The beads are ~1 μm in diameter. The *z* coordinate is aligned with the microscope's optical axis and is normal to the page.

A 1064 nm optical trap [22] was used to capture a 1-μm-diameter bead at each end of an actin filament (Fig. 1). Since macroscopically the filament appeared to be firmly attached to the beads, it is likely that it was linked to the beads by multiple myosin molecules. The forward-scattered infrared light at the back focal plane of the collecting objective was projected onto a quadrant photodiode (Current Designs, Inc.) to measure force [15].

To calibrate the trap, we employed two methods [7,23,13]. In one method, we measured the power spectrum of the bead's thermal fluctuations and compared the measurements with theoretical predictions to obtain the trap's spring constant [24]. In our second calibration method, we oscillated the microscope stage back and forth with a constant velocity and determined the detector's response as a function of the bead's hydrodynamic drag force [24]. The trap stiffness calibration was carried out with every trapped bead immediately prior to each experiment. The trap's spring constant varied from bead to bead, depended on the laser's intensity, and ranged from 0.01 to 0.02 pN/nm.

An electron multiplying charge coupled device (CCD) camera (Andor Technologies) collected images every 2 s, with exposure times of 10, 20, 30, 50, 75, 100, 200, and 300 ms. The camera images were analyzed with a custom MATLAB™ algorithm to determine the filament's instantaneous position [1]. The background signal of each frame was determined by calculating the moving average from square 1 μm × 1 μm regions. The background intensity was subtracted from the image. A straight line, referred to as *E*-*E*, was drawn between the filament's end points. Subsequently, transverse lines, referred to as *T*-*T*, perpendicular to *E*-*E* were erected at ~400 nm intervals. The intensity data along each *T*-*T* line were fitted with a Gaussian curve, and the position of the filament was identified as the centroid of the fitted Gaussian curve. We estimate this technique to have a precision of ±50 nm. The uncertainty in the position measurement was obtained by calculating the standard deviations of the positions of various points along a filament immobilized to a surface.

The bending stiffness of our filaments was determined by measuring the variances of the transverse fluctuations of freely oscillating filaments and analyzing the data with a technique described later in this paper [29]. Since our estimate of the bending rigidity is consistent with the literature value [4], in the interest of space, we omit details.

III. MATHEMATICAL MODEL

We assume the actin filament behaves like a slender elastic beam with uniform elastic modulus E, cross-sectional uniform moment of inertia I, and average tension τ. The product EI is the bending rigidity. We first determine the filament's equilibrium shape and then consider thermal fluctuations about this equilibrium.

A. Filament's static equilibrium shape

Consider an inextensible filament of contour length $2L$ that is connected to two beads subjected to opposing forces of magnitude τ in the x direction (Fig. 1). We use the arc length $\hat{s}$ to specify position along the filament. $\hat{s}=0$ at the filament's midlength $(-L \le \hat{s} \le L)$. The overscript "hat" denotes dimensional quantities that will be later rendered dimensionless. The moment acting on the filament at any position $\hat{s}$ is $M = EI d\theta/d\hat{s}$, where θ is the angle between the tangent to the filament and the x axis. Force equilibrium requires [25]

$$\frac{d^2\theta}{ds^2} - m^2 \sin\theta = 0 \quad (-1 \le s \le 1). \qquad (1)$$

In the above, $m^2 = \tau L^2/EI$, $s = \hat{s}/L$, and L is the length scale. We scaled the force τ with $\tau_c = EI/L^2$. τ_C represents the susceptibility of the beam to bending. It is obtained from order of magnitude estimate based on the constitutive relation $M = EI d\theta/d\hat{s}$ by approximating $M \sim a\tau_c$ and $d\theta/d\hat{s} \sim a/L^2$. τ_c is also proportional to the critical force $[\pi^2 EI/(4L^2)]$ needed to buckle a hinged, Euler beam.

At $s = \pm 1$, balance of moments yields

$$\frac{d\theta(s=\pm 1)}{ds} = m^2\left(\frac{a_\pm}{L}\right)\cos[\theta(s=\pm 1)], \qquad (2)$$

where a is the radius of the bead. The subscripts "+" and "−" denote, respectively, the bead on the right and the bead on the left. For use below, it is convenient to also introduce a Cartesian coordinate system x, y, and z (Fig. 1). The x coordinate is aligned along the line that connects the beads' centers and has its origin at the filament's midpoint. The z coordinate is aligned with the microscope's optical axis and perpendicular to the page.

For conciseness, we focus only on the case when both beads have the same radius $a_+ = a_- = a$. The derivation, however, can be extended straightforwardly to the more general case of $a_- \neq a_+$. In the experiment, the filament and the two beads' centers did not always reside in the same plane. For the purpose of this section, we will consider, however, only the planar case. In the planar arrangement, one can distinguish between the symmetric case $\theta(-s) = -\theta(-s)$ and $\theta(0)=0$ and the antisymmetric case $\theta(-s)=\theta(s)$ and $d\theta(0)/ds=0$. In the interest of space, we derive results only for the former. We will be mostly interested in asymptotic results applicable for moderate and large applied forces (these are the cases that we encounter in the experiments). These asymptotic results are valid for both the symmetric and asymmetric cases.

The first integral of Eq. (1) is

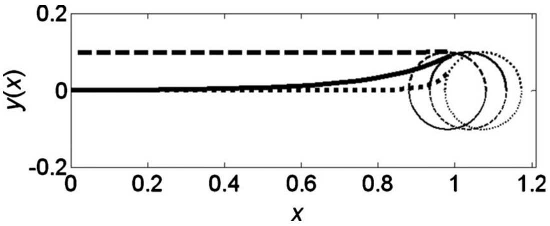

FIG. 2. The equilibrium shapes of filaments ($0<s<1$) when $m=0.2$ (dashed line), 2 (solid line), and 20 (dotted line). $a/L=0.1$. The three circles depict the position of the bead when $m=0.2$ (dashed line), 2 (solid line), and 20 (dotted line). Symmetric boundary conditions are applied to the filament.

$$\frac{1}{2}\left(\frac{d\theta}{ds}\right)^2+m^2\cos\theta=C, \tag{3}$$

where C is a constant of integration. It is instructive to consider the order of magnitude of m. The bending rigidity of actin is estimated as $EI\sim 7\times 10^{-26}$ Nm^2 [4]; the bead radius $a\sim 0.5$ μm; and the actin length $2L\sim 10$ μm. When the trap force τ is on the order of 1 pN, $m^2=400$. Thus, in most circumstances encountered in our optical trap experiments, $m\gg 1$ (i.e., $m>10$).

The exact solution of Eqs. (1) and (2) is in terms of an elliptic integral (Appendix). Figure 2 depicts the static equilibrium shape of the filament in the range $0<s<1$ when $m=0.2$, 2, and 20 and $a/L=0.1$ using the Cartesian coordinates x and y. The coordinates x and y were computed together with the solution of Eq. (1) by solving the equations $dx/ds=\cos[\theta(s)]$ and $dy/ds=\sin[\theta(s)]$ with the boundary conditions $x(0)=0$ and $y(1)=(a/L)\cos[\theta(1)]$. The right bead's center is located at $\{x,y\}=\{\int_0^1\cos[\theta(\xi)]d\xi+a/L\sin[\theta(1)],0\}$. When $m>10$, along a significant fraction of the filament's length, excluding small regions next to the beads, $\theta(s)\sim y(s)\sim 0$. We will take advantage of this fact in the next section.

When m is sufficiently large (i.e., $m\geq 5$ when $a/L=0.1$) allowing one to assume $\theta(0)=d\theta(0)/ds\sim 0$,

$$\theta(s)\sim 4\tan^{-1}\left\{\tan\left[\frac{\theta(1)}{4}\right]e^{m(s-1)}\right\} \tag{4}$$

provides an excellent approximation of the exact solution over the entire domain $-1\leq s\leq 1$. See Appendix, Sec. 3 for the derivation of Eq. (4) and for an expression for $\theta(1)$ [Eq. (A13)].

Equation (4) allows us to readily obtain an asymptotic approximation for the center to center distance between the beads as a function of the dimensionless load m when $m\gg 1$ (see the Appendix):

$$\varepsilon_\ell=\frac{X_{cc}-2}{2}\sim\sqrt{\frac{4EI}{L^2\tau}}\left[\left(u\sqrt{\frac{a^2\tau}{EI}}+1\right)\sqrt{1-u^2}-1\right]. \tag{5}$$

In the above, X_{cc} is the beads' center to center distance and

$$u=\sqrt{\left(\frac{1}{2}+\frac{EI}{4a^2\tau}\right)}-\sqrt{\frac{EI}{4a^2\tau}}. \tag{6}$$

To obtain Eq. (5), we eliminated the last term of Eq. (A15), which contributes insignificantly for moderate and large values of m. When $a/L=0.1$ and $m>1$, the last term in Eq. (5) can be safely neglected. When $m\geq 3$, Eq. (5) is accurate within 0.5%. For additional details as well as other asymptotic approximations for small and large m, see the Appendix.

B. Filament's thermal fluctuations

Next, we consider small fluctuations of the filament about its equilibrium state. Based on the analysis of Sec. III A, at equilibrium and subject to the typical forces applied in the experiments, $y(s)=0$ along most of the filament's length. In our analysis of the thermal fluctuations, we will neglect torsional modes. The filament's motion is projected onto two orthogonal planes. Within the framework of linear elasticity, the motions in each plane can be considered independently. We focus our attention on the plane that is perpendicular to the microscope's optical axis. The transverse dimensionless displacement $\zeta(s,t)$ (normalized with L) of a beam with uniform flexural rigidity EI(Nm^2) linear density ρ(kg/m) and tension τ (N) vibrating in a viscous medium with viscous resistance per unit length $f_\perp$ (Ns/m^2), is given by the dimensionless beam equation [25]:

$$\left(\frac{\rho EI}{f_\perp^2L^4}\right)\frac{\partial^2\zeta}{\partial t^2}+\frac{\partial\zeta}{\partial t}=m^2\left(\frac{\partial^2\zeta}{\partial s^2}\right)-\frac{\partial^4\zeta}{\partial s^4}+\frac{L^3}{EI}F(s,t)$$
$$(-1\leq s\leq 1). \tag{7}$$

In the above, the time t is scaled with $\Lambda=fL^4/EI$; $f_\perp=4\pi\eta/[\ln(2L/a)+0.5]$ [26], η is the suspending fluid's viscosity, and $F(s,t)$ (N/m) is a white, stochastic force per unit length of the filament with an ensemble average

$$\langle F(s,t)\rangle=0 \tag{8}$$

and correlation

$$\langle F(s_i,t_i)F(s_j,t_j)\rangle=\phi(s_i-s_j,t_i-t_j), \tag{9}$$

where ϕ is approximated with the Dirac-Delta function. In the above, $\langle\ \rangle$ denotes an ensemble average.

The boundary conditions require some elaboration. Since we are focusing on the straight segment of the filament, we approximate the filament's ends as if they were free to rotate and specify zero moment conditions at both ends:

$$\frac{\partial^2\zeta(\pm 1,t)}{\partial s^2}=0. \tag{10}$$

When analyzing the experimental data, we measured the displacements relative to a line that connects the filament's ends. Hence,

$$\zeta(\pm 1,t)=0. \tag{11}$$

Boundary conditions (10) and (11) correspond to a beam hinged at both ends. Since the boundary conditions are not precisely known, it is constructive to consider also the other extreme case of a clamped beam,

$$\frac{\partial \zeta(\pm 1,t)}{\partial s}=0, \tag{12}$$

which will provide a lower bound for the estimated tension.

C. Solution of the beam equation

We seek a solution of the form [27]

$$\zeta(s,t)=\sum_{n=1}^{\infty} A_n(t)Y_n(s), \tag{13}$$

where the amplitudes $A_n(t)$ and $A_m(t)$ are temporary uncorrelated for any $n \neq m$, i.e., $\langle A_n(t)A_m(t)\rangle=0$. $Y_n(s)$ are the eigenfunctions of the appropriate Sturm-Liouville boundary value problem (see below) and form a complete orthonormal set. The thermal force is expanded in a similar fashion, i.e., $F(s,t)=\Sigma_{n=1}^{\infty}F_n(t)Y_n(s)$. Substituting Eq. (13) into Eq. (7) and separating variables, we obtain the self-adjoint eigenvalue problem

$$\frac{\partial^4 Y_n}{\partial s^4}-m^2\frac{\partial^2 Y_n}{\partial s^2}-\lambda_n m^4 Y_n=0 \quad (-1\leq s\leq 1), \tag{14}$$

with the boundary conditions

$$Y_n^H(\pm 1)=\frac{\partial^2 Y_n^H(\pm 1)}{\partial s^2}=0 \tag{15}$$

in the hinged case and

$$Y_n^C(\pm 1)=\frac{\partial Y_n^C(\pm 1)}{\partial s}=0 \tag{16}$$

in the clamped case. The superscripts H and C denote, respectively, the hinged and clamped cases and will be used only when it is necessary to distinguish between these two cases. The factor m^4 was introduced in $\lambda_n m^4$ for notational convenience.

For the specified boundary conditions, the eigenmodes $Y_n(s)$ are orthogonal and can be normalized so that

$$\int_{-1}^{1} Y_n(s)Y_m(s)=\delta_{nm}. \tag{17}$$

Equation (14) admits a general solution of the form

$$\begin{aligned}Y_n(s)=C_{n,1}\cosh(z_{1,n}s)+C_{n,2}\sinh(z_{1,n}s)+C_{n,3}\cos(z_{2,n}s)\\ +C_{n,4}\sin(z_{2,n}s),\end{aligned} \tag{18}$$

where

$$z_{1,n}=\frac{m}{\sqrt{2}}(\sqrt{4\lambda_n+1}+1)^{1/2} \quad \text{and} \quad z_{2,n}=\frac{m}{\sqrt{2}}(\sqrt{4\lambda_n+1}-1)^{1/2}. \tag{19}$$

In the case of the hinged beam,

$$Y_n^H(s)=\sin\left(\frac{n\pi}{2}(s+1)\right), \tag{20}$$

$\lambda_n^H=(n\pi/2m)^2(1+(n\pi/2m)^2)$, and n is an integer $(n=1,2,\ldots)$.

In the case of the clamped beam, the eigenvalues are determined by the solution of the characteristic equation:

$$\begin{aligned}4\sqrt{\lambda_n^C}[\cosh^2(z_{1,n})\cos(2z_{2,n})-\cos^2(z_{2,n})]\\ -\sinh(2z_{1,n})\sin(2z_{2,n})=0.\end{aligned} \tag{21}$$

For moderate values of λ_n, Eq. (21) can be approximated with the equation

$$\tan(2z_{2,n})-4\sqrt{\lambda_n^C}=0. \tag{22}$$

When λ_n is even larger,

$$\lambda_n^C \approx \left[\frac{(2n+1)\pi}{4m}\right]^2\left\{\left[\frac{(2n+1)\pi}{4m}\right]^2+1\right\}. \tag{23}$$

For example, when $m=1.25$, the first few exact eigenvalues [Eq. (21)] are {14.78, 104.73, 390.03,…}. The first implicit approximation [Eq. (22)] gives {15.41, 106.02, 391.79,…} and the second explicit approximation Eq. (23)] yields {16.18, 107.23, 393.55,…}. The eigenfunctions are

$$\begin{aligned}Y_n^C(s)=C^*\left\{\frac{\cosh[z_{1,n}(s+1)]-\cos[z_{2,n}(s+1)]}{\cosh(2z_{1,n})-\cos(2z_{2,n})}\right.\\ \left.-\frac{z_{2,n}\sinh[z_{1,n}(s+1)]-z_{1,n}\sin[z_{2,n}(s+1)]}{z_{2,n}\sinh(2z_{1,n})-z_{1,n}\sin(2z_{2,n})}\right\},\end{aligned} \tag{24}$$

where the constant C^* is selected to render the norm $\|Y_n^C(s)\|=1$.

According to the principle of equipartition of energy, the elastic energy associated with each mode

$$\begin{aligned}U_n&=\frac{\langle A_n^2(t)\rangle}{2}\int_{-1}^{1}\left[\frac{EI}{L}\left(\frac{\partial^2 Y_n}{\partial s^2}\right)^2+\tau L\left(\frac{\partial Y_n}{\partial s}\right)^2\right]ds\\ &=\frac{EI}{2L}\langle A_n^2(t)\rangle\int_{-1}^{1}\left[\left(\frac{\partial^2 Y_n}{\partial s^2}\right)^2+m^2\left(\frac{\partial Y_n}{\partial s}\right)^2\right]ds\end{aligned} \tag{25}$$

equals $k_BT/2$, where k_B is the Boltzmann constant and T is the absolute temperature. Using Eq. (14), the boundary conditions and the orthonormality of the eigenvectors, we have

$$U_n=\frac{EI}{2L}\langle A_n^2(t)\rangle\lambda_n m^4 \tag{26}$$

or $\langle A_n^2(t)\rangle=k_BTL/EI1/\lambda_n m^4$.

The variance of the transverse fluctuations is

$$V_{\text{th}}(s)=\langle[\zeta(s,t)-\langle\zeta(s,t)\rangle]^2\rangle=\sum_{n=1}^{\infty}\langle A_n(t)^2\rangle[Y_n(s)]^2, \tag{27}$$

where the subscript “th” denotes theoretical estimate.

In the hinged case,

$$V_{\rm th}^{H}(s)=\frac{16k_BTL}{EI}\sum_{n=1}^{\infty}\frac{1}{(n\pi)^2[4m^2+(n\pi)^2]}\sin^2\left[\frac{n\pi}{2}(s+1)\right]. \tag{28}$$

The rate of convergence of the above series depends on the magnitude of m. When $m=2$, two terms in the series approximate the variance within 1%. When $m=20$, eleven terms are needed to obtain the same level of approximation. Fortunately, Eq. (28) can be summed-up in closed form to give

$$V_{\rm th}^{H}(s)=\frac{k_BTL}{2m^2EI}\left((1-s^2)-\frac{\cosh(2m)-\cosh(2ms)}{m\,\sinh(2m)}\right). \tag{29}$$

The first term on the right $k_BTL/2m^2EI(1-s^2)$ is the variance of a fluctuating string with tension τ. The second term represents the reduction in the variance due to the flexural rigidity. The second term decays as m increases. When $m \gg 1$, Eq. (29) has the asymptotic approximation

$$V_{\rm th}^{H}(s)\sim\frac{k_BT}{2\tau L}\left\{(1-s^2)-\frac{1}{m}[1-e^{-2m(1-|s|)}]\right\} \quad (m\gg 1). \tag{30}$$

The corresponding expressions for the clamped case are considerably lengthier, were computed numerically, and are not reproduced here. Note that, consistent with the equipartition theorem, the variance is independent of the suspending liquid's viscosity.

D. An inverse problem: Estimation of the filament's tension

We use the experimentally observed transverse variance to estimate the filament's tension. To this end, we consider the theoretical variance to be a function of the filament's tension, and we seek the tension τ that minimizes the discrepancy

$$\Theta(\tau)=\frac{1}{N}\sum_{i=1}^{N}[V_{\rm th}(s_i,\tau,\kappa)-V_{\rm exp}(s_i,\tau,\kappa)]^2, \tag{31}$$

between theoretical predictions $V_{\rm th}(\tau)$ and experimental observations $V_{\rm exp}$. In the minimization process, we used the flexural rigidity $EI=7.3\times10^{-26}$ Nm^2 of actin filaments [4]. In independent measurements (not described here), we obtained a similar value for the flexural rigidity [29].

For example, Fig. 3 depicts $\Theta(\tau)$ as a function of τ for applied trap forces $\tau_{\rm applied}=0.21$ pN (solid line), 0.36 pN (dashed line), and 0.80 pN (dash-dotted line). The respective, estimated forces (the minima of the curves) are 0.23, 0.39, and 1.2 pN. The filament's length is 15 μm. Witness that the curves are convex and have deep, global minima allowing one to estimate the tension force within ±20%. At low applied forces (<0.39 pN), the discrepancy between the estimated force and applied force is ~10%. The discrepancy increases as the applied force increases.

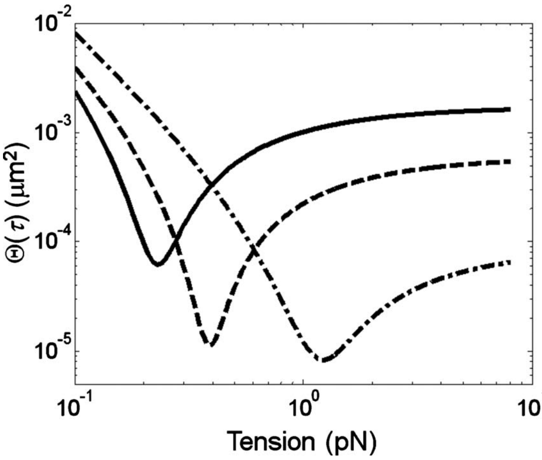

FIG. 3. The average error $\Theta(\tau)$ depicted as a function of the filament's tension τ when $\tau_{\rm applied}=0.21$ pN (solid line), 0.36 pN (dashed line), and 0.80 pN (dash-dotted line). The corresponding estimated forces were, respectively, 0.23, 0.39, and 1.2 pN. The filament's length is 15 μm.

IV. RESULTS AND DISCUSSION

A. Effect of camera exposure time on variance measurement

In the course of our experiments, the filament vibrated relative to the camera. As a result, blurring of the image was unavoidable. The impact of this phenomenon depended on the relative magnitude of the camera's exposure time t_e compared with the characteristic time of the filament's fluctuations $\hat{t}$. As $t_e/\hat{t}$ increased, the variance estimated from the experimental data decreased, and the filament tension τ, estimated without correcting for the blurring, increased.

1. Theoretical considerations

Recently, Towles *et al.* [28] demonstrated that the measured variance of a tethered bead undergoing Brownian motion decreases as the camera's exposure time increases. In other words, the bead's measured position is biased toward its mean position. Here, we carry out similar analysis for the case of a vibrating filament. From Eq. (7), neglecting inertia, we have the Langevin equation for the amplitudes (A_n)

$$\frac{dA_n}{dt}=-\lambda_n m^4 A_n+\frac{L^3}{EI}F_n(t), \tag{32}$$

which admits the solution

$$A_n(t)=A_n(0)e^{-\lambda_n m^4 t}+\frac{L^3}{EI}\int_0^t F_n(u)e^{\lambda_n m^4(u-t)}du. \tag{33}$$

We carry out the integration for sufficiently long time to allow the effect of the initial condition [the first term on the right-hand side of Eq. (33)] to decay. The amplitude observed by the camera is the average amplitude over the exposure time t_e.

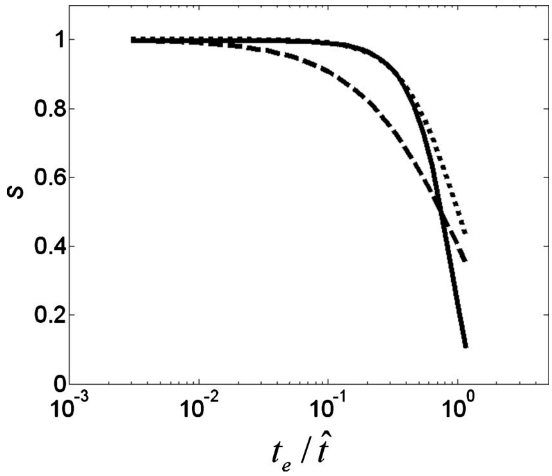

FIG. 4. The correction factor $S(t_e)$ as a function of the normalized exposure time $t_e/\hat{t}$ when $F_1(t)=\sin(\omega t)$ and $F_{n>1}=0$. $\lambda=4$, $m=1$, and $\omega=1$. The solid, dashed, and dotted lines correspond, respectively, to the exact calculation, a fit obtained with Eq. (37), and a fit obtained with Eq. (38).

$$A_n^{\mathrm{CAMERA}}(t) = \frac{L^3}{t_e EI}\int_t^{t+t_e}\int_0^t F_n(u)e^{\lambda_n m^4(u-v)}du dv. \tag{34}$$

The time constant associated with mode n is $\hat{t}_n=1/\lambda_n m^4$. When n is small and m is moderate, the "string modes" dominate, $\hat{t}\propto\tau^{-1}$, and the vibration's time constant decreases as the filament's tension increases. When $n \gg 1$, the flexural (bending) modes dominate and the time constant is independent of the filament's tension.

To compute the variance of any variable X, we calculate the integral

$$V_X = \lim_{t\to\infty}\frac{1}{t}\int_0^t X^2(z)dz. \tag{35}$$

We define the ratio between the variance constructed using the camera images and the true variance as

$$S(t_e) = \frac{V_A^{\mathrm{CAMERA}}(t_e)}{V_A^{TRUE}}. \tag{36}$$

Unfortunately, $S(t_e)$ depends on the thermal force and does not lend itself to a simple expression. Figure 4 (solid line) illustrates the behavior of $S(t_e)$ as a function of the normalized exposure time $t_e/\hat{t}$ when the force $F_1(t)=\sin(\omega t)$ and $F_{n>1}=0$ (solid line). Witness that when $t_e/\hat{t}>1$, $S(t_e)$ decreases rapidly as $t_e/\hat{t}$ increases.

For the fluctuating bead, Towles *et al.* [28] proposed a correction factor of the form

$$S(t_e) = \left[\frac{\hat{t}}{t_e}(1-e^{-t_e/\hat{t}})\right]^2, \tag{37}$$

where the time constant $\hat{t}$ is determined empirically. Although expression (37) provides qualitatively correct behavior, its quantitative predictions (dashed line in Fig. 4) do not match well the predictions of Eq. (36) (solid line) for the filament fluctuations. We find that, in the range of interest, the computed data of Fig. 4 correlates better with an expression of the form (dotted line)

$$S(t_e) = \frac{1}{1+\left(\frac{t_e}{\hat{t}}\right)^{\gamma}}, \tag{38}$$

where $\gamma\sim 1.8$ provided the best fit when the forcing function $F_1(t)=\sin(\omega t)$. Expression (38), which resembles the transfer function of a low pass filter, may need to be modified when other forcing functions are used.

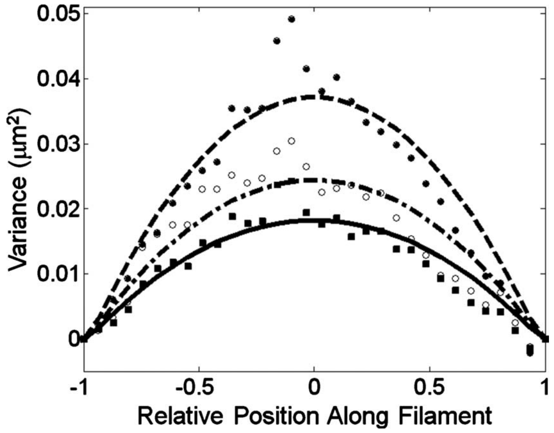

FIG. 5. The variance is depicted as a function of position along a 17-μm-long filament when the camera exposure time is 75 ms (solid circles, dashed line), 200 ms (hollow circles, dashed-dot line), and 300 ms (squares, solid line). The various lines correspond to theoretical fits with hinged boundary conditions. $\tau_{\mathrm{applied}}=0.26$ pN.

2. Experimental observations

To examine the effect of the camera's exposure time on the estimate of the thermal vibration's variance, we carried out a sequence of measurements of the filament's vibrations as we modified the camera's exposure time. Figure 5 depicts the variance (symbols) as a function of position along a 17-μm-long filament suspended in water for camera exposure times $t_e=75$ ms (solid circles), 200 ms (hollow circles), and 300 ms (squares) The applied trap force $\tau_{\mathrm{applied}}=0.26$ pN. We fitted the experimental data with theoretical fits based on the hinged model (lines). As the exposure time t_e increased, the variance decreased, and the estimate for the force increased.

The effect of the camera exposure time on the variance is summarized in Fig. 6. The figure depicts the normalized variance integrated along the filament's length (symbols) as a function of the camera's exposure time for three different filaments. The variance was normalized with the estimated true variance. The solid squares and solid triangles correspond to filaments suspended in 60% (by mass) glycerin ($\eta=10.8$ mPa s) solution. The glycerin was used to increase the filaments' vibration time constant. The solid squares correspond to a 15-μm-long filament subjected to a 0.3 pN force (filament A). The solid triangles correspond to a

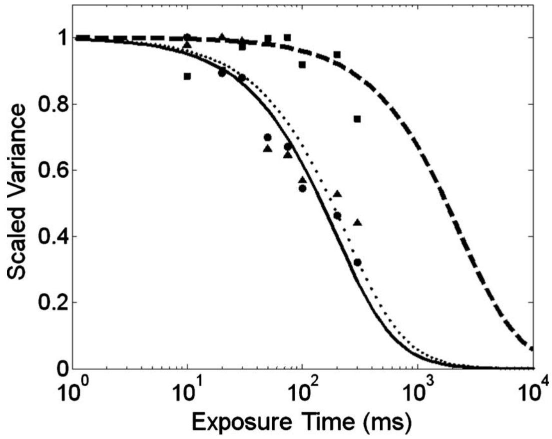

FIG. 6. The normalized, experimental variance is depicted as a function of the camera exposure time. The solid circles, solid triangles, and solid squares correspond, respectively, to $\{L, \tau_{\text{applied}}, \eta\} = \{17\ \mu\text{m}, 0.3\ \text{pN}, 1\ \text{mPa s}\}$, $\{12\ \mu\text{m}, 1.2\ \text{pN}, 10.8\ \text{mPa s}\}$ and $\{15\ \mu\text{m}, 0.3\ \text{pN}, 10.8\ \text{mPa s}\}$. In the above, L, τ, and η represent, respectively, the filament's length, the applied tension, and the suspension's viscosity. The measured variance was normalized with its largest value. The solid, dotted, and dashed lines correspond to predictions based on Eq. (38).

12-μm-long filament subjected to a 1.2 pN tension force (filament B). The solid circles correspond to a 17-μm-long filament suspended in water and subjected to 0.3 pN of trap force (filament C). Unfortunately, due to camera sensitivity limitations and fluorescent bleaching, respectively, it was not always possible to obtain short and long exposure time data.

We first discuss the data associated with filaments A and B suspended in glycerin (solid squares and solid triangles). When the exposure time is relatively small, the measured variance is scattered about a horizontal line. The variance associated with the short time plateau ($V_{\text{exp},0}$) is independent of the exposure time and represents the true variance of vibrations. We used $V_{\text{exp},0}$ to normalize the data presented in Fig. 6. The predicted dimensional time constant associated with the fundamental modes of vibrations of filaments A and B are, respectively, $\tilde{t}_1 = \Lambda \hat{t}_1 = fEI/\lambda_1 \tau^2 = 1200$ and 160 ms. We estimate the time constants associated with filament C to be 130 ms. Hence, we speculate that the lowest available exposure time of 10 ms is sufficiently small to provide a reasonable measure of the true variance $V_{\text{exp},0}$. Accordingly, we normalized filament C's data with the variance measured at the shortest available exposure time. Next, we fitted all the experimental data with a curve based on Eq. (38). In the fitting process, we used the theoretical estimates of the time constants. The exponent $\gamma = 1.1$ provided the best fit. The dashed line, dotted line, and solid line correspond, respectively, to the predictions of Eq. (38) ($\gamma = 1.1$) with the theoretical time constants of filaments A, B, and C.

In summary, the measured variance depends sensitively on the camera exposure time. To obtain a reasonable estimate of the variance, the camera exposure time t_e must be significantly smaller than the filament's time constant $\hat{t}$. In Fig. 6, this was the case only for the filaments suspended in glycerin. The figure depicts the experimental estimate of S [Eq. (38)] as a function of the camera exposure time. It suggests that Eq. (38) (with $\gamma = 1.1$) can be used to correct long exposure time experimental data.

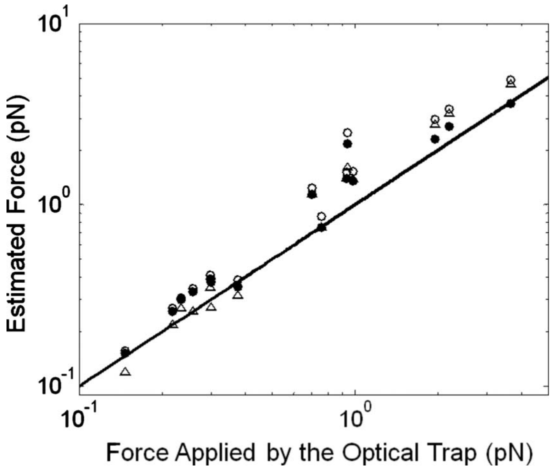

FIG. 7. The force estimated for 6 filaments (in glycerin, $\eta = 10.8$ mPa s), depicted as a function of the applied force. The hollow circles, solid circles, and triangles correspond, respectively, to the predictions of the uncorrected hinged model, corrected hinged model, and uncorrected clamped model. The solid line represents a 1:1 correlation between actual and estimated force values.

B. Estimates of the filament's tension based on the variance of the transverse fluctuations calculated from the filament's instantaneous position

Since we were not able to sufficiently reduce the camera exposure time for the experiments carried out in water to obtain accurate estimates of the variance, we report in this section mostly on results of experiments carried out with filaments suspended in a glycerin-water mixture. Since the viscosity of the glycerin-water mixture was about ten times larger than that of water, the time constant of the fluctuations was increased by an order of magnitude. All the measurements were carried out with a camera exposure time of 30 ms. This exposure time provided a reasonable compromise between the opposing needs of good sensitivity and minimal blurring.

The data processing involved measuring the thermal fluctuations' variance as a function of position along the filament to obtain curves similar to the ones depicted in Fig. 5. These experimental data were then fitted with the theoretical curves of the hinged and clamped models to obtain estimates of filament tension. Calculations were carried out using both the uncorrected and corrected [Eq. (38)] variances. Figure 7 summarizes the Brownian dynamics model-based estimates of filament tension as a function of the applied optical trap force. The hollow circles, solid circles, and hollow triangles correspond, respectively, to the predictions of the uncorrected hinged model, corrected hinged model, and uncorrected clamped model. The correction consisted of dividing the variance by the factor S from Fig. 6. The time constant was adjusted to reflect each filament's experimental conditions. The solid line is a 45° line. At relatively low forces (<0.7 pN), the uncorrected and corrected estimates of the

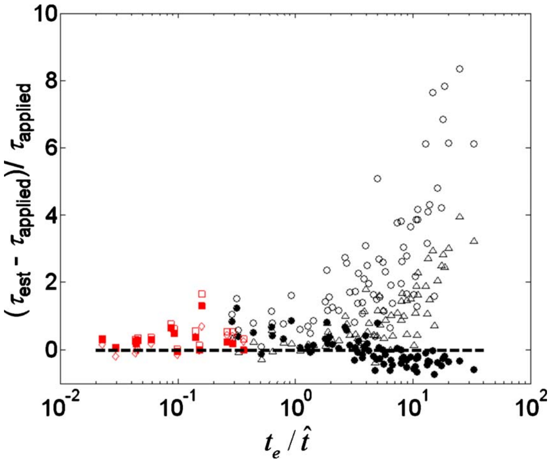

FIG. 8. (Color online) The relative discrepancy between the estimated force and the applied force as a function of the filament's time constant associated with the fundamental mode of vibration ($n=1$) for filaments suspended in glycerin (red squares and diamonds) and filaments suspended in water (black circles and triangles). The hollow circles (and squares), solid circles (and squares), and triangles (and diamonds) correspond, respectively, to the predictions of the uncorrected hinged model, corrected hinged model, and uncorrected clamped model.

hinged filament tension are in good agreement (<30%) with the applied trap forces. As the magnitude of the force increased, so did the discrepancy between the uncorrected estimated forces and the applied optical trap forces. This increase in the discrepancy is attributed to a reduction in the filament's time constant as the force increases. When $1\ \text{pN} < \tau_{\text{applied}} < 4\ \text{pN}$, $\tau_{\text{applied}} < \tau_{\text{estimated,uncorrected}} < 1.7\ \tau_{\text{applied}}$ (hollow circles) and $\tau_{\text{applied}} < \tau_{\text{estimated,corrected}} < 1.3\ \tau_{\text{applied}}$ (solid circles) (excluding a few outliers). Not surprisingly, the clamped model-based estimates are lower than those of the hinged model-based estimates and in some cases underestimate the trap force.

Figure 8 depicts the relative discrepancy between the estimated force and the applied force as a function of the camera exposure time normalized with the filament's theoretical time constant (fundamental mode) $t_e/\hat{t}_1$. The figure includes data for both filaments suspended in glycerin (red squares and diamonds) and filaments suspended in water (black circles and triangles). The hollow circles (and squares), solid circles (and squares), and triangles (and diamonds) correspond, respectively, to predictions of the uncorrected hinged model, the corrected hinged model, and the uncorrected clamped model. The distribution of filament lengths in our experiments was quite narrow ($12.2 \pm 3.0\ \mu\text{m}$). Shorter filaments had a characteristic time scale too short for observation, and longer filaments were difficult to find.

Not surprisingly, as $t_e/\hat{t}_1$ increases, the discrepancy between the uncorrected estimated force and the actual force increases. When $t_e/\hat{t}_1 < 0.1$, the discrepancy between the estimated force (hinged model) and applied force was smaller than 60%. Since our method typically underestimates the variance, we tend to overestimate the force. For the entire range of our measurements, $0.5\ \tau_{\text{applied}} < \tau_{\text{estimated,corrected}} < 1.5\ \tau_{\text{applied}}$

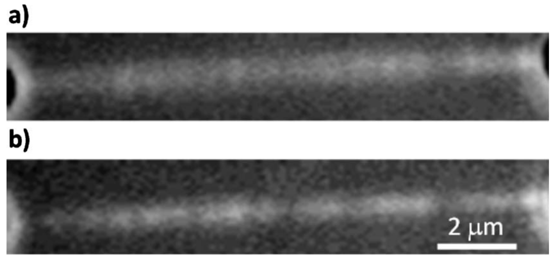

FIG. 9. Blurred images of an 11-μm-long filament as recorded by the camera for a cumulative exposure time of 10 s when (a) $\tau_{\text{applied}}=0.22$ pN and (b) 0.93 pN.

C. Estimates of the filament's tension based on the variance of the transverse fluctuations obtained from long exposure

As an alternative technique to estimate the filament's variance, we took long exposure time images of the filament (or, alternatively, superposed many images taken with various exposure times.) In other words, in contrast to the previous section where our objective was to go to the limit of short exposure time $(t_e/\hat{t}_1) \to 0$, here we explore the limit of long exposure time $(t_e/\hat{t}_1) \to \infty$. Figure 9 provides representative blurred images of an 11-μm-long filament subject to applied tensions of 0.22 pN (a) and 0.93 pN (b) as recorded by the camera for a cumulative exposure time of 10 s. Witness that the width of the "blur" decreased as the filament's tension increased.

To determine the variance, we used a procedure similar to the one described in Sec. II. The fluorescent emission intensity was measured along several uniformly spaced lines perpendicular to the line connecting the filament's end points. Figure 10 depicts two such normalized emission intensity profiles, after subtracting background emission intensity, as functions of the transverse position when the applied tension is 0.22 pN (solid circles) and 0.93 pN (solid squares). The emission intensity was normalized with its maximum value. The experimental data were fitted with Gaussian curves with

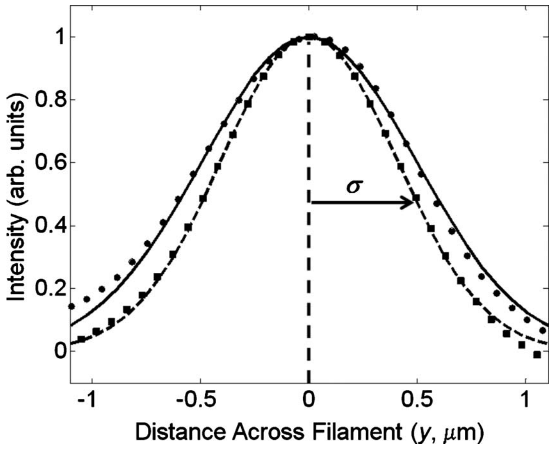

FIG. 10. The normalized light intensity is depicted transverse to the 11-μm-long filament at the filament's midlength when $\tau_{\text{applied}}=0.22$ pN (circles, solid line), 0.93 pN (squares, dashed line). The symbols and solid lines correspond, respectively, to experimental data and Gaussian fits.

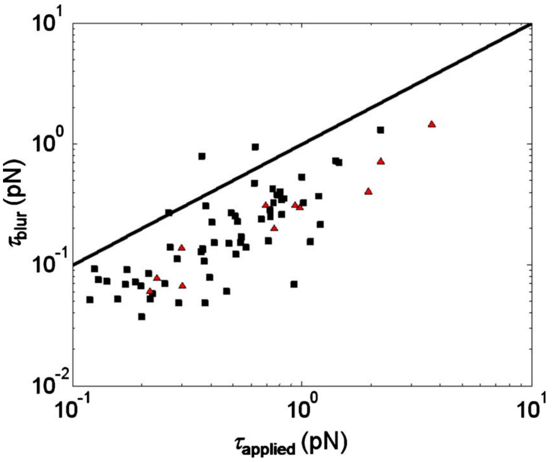

FIG. 11. (Color online) The "blur variance" force estimates for hinged conditions (symbols) depicted as a function of the applied force. The triangles and the squares correspond, respectively, to filaments suspended in glycerin and water. The solid line represents a 1:1 correlation between actual and estimated force values.

the blur variance σ_{blur}^2 as the fitting parameter. The blur variances of the images of the filament's left and right ends were denoted, respectively, $\sigma_{\text{blur},L}^2$ and $\sigma_{\text{blur},R}^2$. The average variance $(\sigma_{\text{blur},L}^2+\sigma_{\text{blur},R}^2)/2$ was subtracted from σ_{blur}^2 to partially correct for the contribution of the beads' rotations and the spreading of light due to the point spread function.

We estimated the filament's tension by minimizing the discrepancy between the corrected blur-variance and the theoretically predicted one. Figure 11 depicts the blur-variance force estimate as a function of the applied force (symbols). The triangles and the squares correspond, respectively, to filaments suspended in glycerin and in water. In contrast to the technique described in Sec. IV B, the blur technique tends to overestimate the filament's variance and to underestimate the force that acts on the filament. The mean errors of the water and glycerin experiments were, respectively, 0.4 and 1.0 pN. That the error in the water experiments was smaller than in the glycerin experiments shows that the exposure time did not have a significant effect on the blurred image-based force estimates.

D. Estimates of the filament's tension based on the variance of the oscillatory modes' amplitudes

We also estimate the filament's tension by analyzing the amplitudes of individual, oscillatory modes. Using Eq. (20), we decompose the filament's shape into the orthogonal modes

$$Y(s) = \sum_n A_n \sin\left(\frac{n\pi}{2}(s+1)\right). \tag{39}$$

The filament's length is divided into segments of length Δs_k, and the amplitudes are computed with the formula

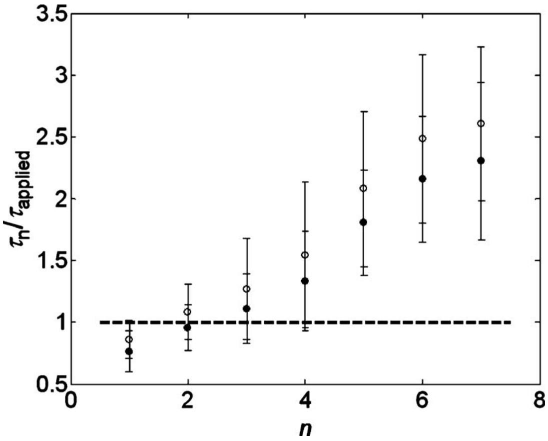

FIG. 12. The tension τ_n estimated from individual modes (n) using Eq. (24) normalized by the applied tension τ_{applied} for 12 filaments suspended in glycerin depicted as a function of mode number. The vertical bars correspond to +/− standard deviation. The hollow and solid circles correspond, respectively, on the estimates based on the uncorrected hinged model and the corrected hinged model.

$$A_n = \sum_k Y_k \Delta s_k \sin\left(\frac{n\pi}{2}(s_k^{mid}+1)\right), \tag{40}$$

where s_k^{mid} is the position of the midpoint of the kth segment. With the aid of Eq. (26), we relate the nth mode amplitude's variance to the applied tension. The variances of the amplitudes of individual modes provide independent estimates of the tension. However, as the mode number increases, the precision of the data deteriorates. Figure 12 depicts the tension τ_n, estimated from individual modes using Eq. (26), normalized by the applied tension τ_{applied}, for 12 filaments suspended in glycerin as a function of mode number. The vertical bars correspond to +/− one standard deviation. The hollow circles and solid circles correspond, respectively, to uncorrected hinged model data and corrected hinged model data. The results of the mode-based analysis are in reasonable agreement with the applied tension for the first few modes. As the mode number increases, the time constant associated with the mode decreases and the measurement error increases. Since the correction is based on the time constant associated with the fundamental mode, it was ineffective in correcting higher modes' data.

V. CONCLUSIONS

Snapshots of actin filaments fluctuating in both water and glycerin were collected as a function of time, applied (measurable) optical trap force, and camera exposure time. The data were analyzed to obtain the transverse displacement variance of the filaments' fluctuations as a function of the applied force, the position along the filament, and the camera exposure time and to obtain the variance of the amplitude of individual Fourier modes. Due to the relatively small time constant of the tensed filaments' fluctuations, the instantaneous displacement method provided usable (uncorrected) data only for filaments suspended in glycerin. The range of utility of the technique can be expanded by correcting the data for blurring. At relatively low forces (<1 pN), both the uncorrected and corrected estimates of the tension of filaments suspended in glycerin were within 50% of the applied trap force. When $\tau > 1$ pN, the discrepancies between the uncorrected and corrected data and the direct optical trap measurements were within a factor of two. The uncorrected data consistently overestimated the filaments' tension providing an upper bound for the force.

To overcome the limitation imposed by the camera's exposure time, an alternative technique was employed in which the fluctuation's variance was estimated from blurred images obtained with lengthy exposure times. By comparing the experimentally measured variances with the predictions of a linear Brownian dynamics model, we estimated the filaments' tensions. The estimated filament tensions agreed with the known applied forces to within 20–70 %. When using the instantaneous displacement method with an applied force smaller than 0.2 pN, the discrepancy between the estimated and applied force is smaller than 20%, which is of the same order of magnitude as the precision of the calibration of the optical trap. As the applied force increased so did the discrepancy between the estimated and applied force. When the applied force was smaller than 2 pN, the estimated force was within a factor of two of the applied force. The increase in estimation error as the force increases is attributed to the decrease in the filament's time constant. Overall, the blur method proved to be less accurate than the instantaneous displacement method. The blur method consistently underestimated the filament's tension. Although both methods, the variance estimate based on the filament's instantaneous position and the blur analysis, use the same data, the two methods process the data differently and use different corrections. Hence, the estimates for the tension obtained with these two techniques are different.

The experiments verify that the methods of statistical mechanics can be used to estimate tension in filaments anchored at both ends. Our experiments provide additional evidence that the methods of statistical mechanics and the principle of equipartition of energy are applicable to mesoscopic structures. The principle of equipartition can be used, however, only in the context of small fluctuations when linear models are applicable. Some of the discrepancy between the experimental data and theoretical predictions could perhaps be attributed to the filaments' departure from linear behavior. However, at low applied forces when the amplitude of the filament's vibrations is relatively large, the departure from linear behavior is most acute and the experimental error is smallest (due to the relatively large time constant of the system), we obtained a good agreement between theoretical estimates and experimental observations, it is likely that the discrepancies between theory and experiment were mostly caused by experimental errors and not departures from linearity.

Finally, the experiments highlighted the importance of adjusting the camera exposure time to reduce blurring effects. When the exposure time is significantly larger than the time constant of the filament's fluctuations, a significant error occurs in estimating the filament's position, which, in turn, results in underestimating the variance of the transverse fluctuations and overestimating the filament's tension.

ACKNOWLEDGMENTS

The work was supported, in part, by the National Science Foundation through the Nano/Bio Interface Center (Grant No. NSF NSEC DMR-0425780) and NIH PPG Grant No. P01GM087253.

APPENDIX: THE FILAMENT'S EQUILIBRIUM CONFIGURATION AND THE SYSTEM'S SPRING CONSTANT

Our objective in this appendix is to derive closed form, approximate expressions for θ and the beads' center-to-center distance as a function of the tension m. To assess the range of validity of the approximate expressions, we first derive the exact solution. In the interest of space, we consider only the symmetric case $\theta(0)=0$.

1. Exact solution

Upon integrating Eq. (3), we have

$$\int_0^{\theta} \frac{d\varphi}{\sqrt{2(C - m^2 \cos \varphi)}} = s, \tag{A1}$$

where the constant of integration $C=m^2(\cos \theta(1) + 1/2m^2(a/L)^2\cos^2 \theta(1))$ is determined with the aid of boundary condition (2). The integral on the right-hand side of Eq. (A1) can be rewritten as the incomplete elliptic integral of the first kind: $\sqrt{2/C-m^2}F(\theta/2, 2m^2/m^2-C)$. $\theta(1)$ is obtained by solving the transcendental equation

$$\int_0^{\theta(1)} \frac{d\varphi}{\sqrt{2(C - m^2 \cos \varphi)}} = 1. \tag{A2}$$

The beads' center-to-center distance is

$$X_{cc} = 2\int_0^1 \cos[\theta(\xi)]d\xi + 2\frac{a}{L}\sin[\theta(1)]. \tag{A3}$$

With the aid of Eq. (3), we rewrite Eq. (A3) in a form more convenient for numerical calculations.

$$X_{cc} = \frac{2}{m}\int_0^{\theta(1)} \frac{\cos \varphi d\varphi}{\sqrt{2[\cos \theta(1) - \cos \varphi] + m^2\left(\frac{a}{L}\right)^2 \cos^2 \theta(1)}} + 2\frac{a}{L}\sin[\theta(1)]. \tag{A4}$$

We solve the integral Eq. (A2) numerically to obtain $\theta(1)$. The solution process runs into difficulties when m is large since the integral readily diverges. Fortunately, for moderate and large values of m, one can obtain accurate asymptotic formulas, as we show shortly.

2. Small m approximation

When $m \ll 1$, one anticipates that the angle θ is small as well. Accordingly, we expand the trigonometric functions in

Eqs, (A1) and (A2) into their corresponding Taylor series about $\theta=0$ and retain terms up to $O(\theta^4)$. This allows us to evaluate the integrals in closed form and obtain

$$\theta(1) \sim \left(\frac{a}{L}\right) m \tanh(m). \tag{A5}$$

Although Eq. (A5) is strictly valid only for $m \ll 1$, it turns out to be surprisingly accurate even for moderate values of m. When $a/L=0.1$ and $m \leq 1$, formula (A5) approximates $\theta(1)$ within 0.3%. When $a/L=0.1$ and $m \leq 3$, the precision is better than 4%. The corresponding asymptotic approximation for the angle $\theta(s)$ is

$$\theta(s) \sim m\left(\frac{a}{L}\right)\frac{\sinh(ms)}{\cosh(m)}, \tag{A6}$$

and for the relative extension, it is

$$\varepsilon_\ell \sim \frac{X_{cc}-2}{2} = \frac{L}{am^2}\cosh(m)\sin\left(\frac{a}{L}m^2 \operatorname{sech}(m)\right) + \frac{a}{L}\sin\left(\frac{a}{L}m \tanh(m)\right) - 1. \tag{A7}$$

When $a/L=0.1$ and $m<3$, Eq. (A7) is accurate within 2%. Equation (A7) can be approximated with $\varepsilon_\ell \sim (a/L)^2 m \tanh(m) \sim (a/Lm)^2 = a^2\tau/EI$. When m is small, most of the contribution to the increase in the distance between the beads' centers comes from the beads' rotation [the second term in Eq. (A3)].

3. Large *m* approximation

In the symmetric case, when $|s| \ll 1$ and $ma/L \gg 1$, $\theta(0)=d\theta(0)/ds \sim 0$. Thus, from Eq. (3), we conclude that the integration constant $C \sim m^2$, and Eq. (3) can be rewritten as

$$\frac{d\theta}{ds} = 2m \sin\left(\frac{\theta}{2}\right). \tag{A8}$$

Equation (A8) can be readily integrated to yield

$$\theta(s) = 4 \tan^{-1}\left\{\tan\left[\frac{\theta(1)}{4}\right]e^{m(s-1)}\right\}, \tag{A9}$$

where

$$\theta(1) = 2 \sin^{-1} u \tag{A10}$$

and

$$u = \frac{\sqrt{2}}{2}\sqrt{\left[1+\frac{1}{2m^2}\left(\frac{L}{a}\right)^2\right]} - \frac{L}{2ma}. \tag{A11}$$

When $m \gg 1$,

$$\theta(1) \sim \frac{\pi}{2} - \sqrt{2}\left(\frac{L}{ma}\right) + \left(\frac{L}{ma}\right)^2 + O\left(\frac{L}{ma}\right)^3. \tag{A12}$$

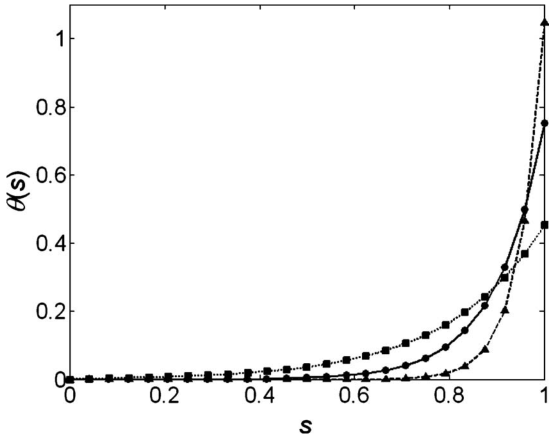

FIG. 13. The displacement angle θ is depicted as a function of the position along the filament (s). Comparison of the approximate, closed form [solid line—Eq. (A8)] and finite element (circles) solutions when $m=5$ (squares), $m=10$ (circles), and $m=20$ (triangles).

When $m\frac{a}{L} \to \infty$, $\theta(1) \to \pi/2$. Although Eq. (A12) is strictly correct only when $m \gg 1$, it is, nevertheless, instructive to obtain an approximation for small m values. When $m \ll 1$, Eq. (A10) reduces to

$$\theta(1) \sim \left(\frac{ma}{L}\right) - \frac{11}{24}\left(\frac{ma}{L}\right)^3 + O\left(\frac{ma}{L}\right)^5. \tag{A13}$$

Equation (A13) provides the correct limit of $\theta(1)=0$ when $m=0$, but it does not provide an adequate description of $\theta(1)$ since the exact solution mandates that $\theta(1)=O(m^2)$ for small m values.

To appreciate how well the asymptotic approximation [Eq. (A10)] performs, we compare its predictions with the exact values for the case of $a/L=0.1$. When $m=2$, Eq. (A10) is accurate within 3.6%. The error decreases rapidly as m increases. When $m>5$, the discrepancy between the exact and approximate values of $\theta(1)$ is smaller than 0.001%.

Figure 13 depicts θ as a function of s when $a/L=0.1$ and $m=5$ (squares), $m=10$ (circles), and $m=20$ (triangles). The symbols and solid line correspond, respectively, to the "exact" and approximate [Eq. (A9)] expressions. Witness the excellent agreement between the approximate and exact expressions.

Upon inserting Eq. (A9) in the integral [Eq. (A3)], we obtain the asymptotic expression for the center-to-center distance:

$$X_{cc} = 2\left\{1+\frac{a}{L}\sin[\theta(1)]\right\} + \frac{4}{m}\left\{1+\cos\left[\frac{1}{2}\theta(1)\right]\right\} - \frac{8}{m\left\{1+e^{-2m}\tan^2\left[\frac{1}{4}\theta(1)\right]\right\}}. \tag{A14}$$

Using trigonometric identities, Eq. (A14) is rewritten as

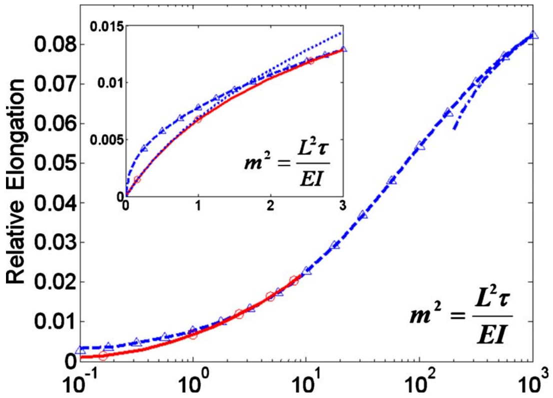

FIG. 14. (Color online) The relative extension $\varepsilon_l = (X_{cc}-2)/2$ is depicted as a function of the dimensionless force m^2 when $a/L = 0.1$. The exact solution $(0 < m < 3)$ is depicted with a solid line with circles. The dashed line with the triangles corresponds to the asymptotic solution [Eq. (A14)]. The dotted line (inset only) corresponds to the small m asymptote Eq. (A6). The dash-dot line (main figure only) corresponds to the very large m approximation Eq. (A15).

$$\varepsilon_\ell = \frac{X_{cc}-2}{2} = \frac{2}{m}\left[\left(\frac{ma}{L}u+1\right)\sqrt{1-u^2}-1\right] + \frac{4}{m}\frac{e^{-2m}(1-\sqrt{1-u^2})}{[1+e^{-2m}+(1-e^{-2m})\sqrt{1-u^2}]}. \tag{A15}$$

When $a/L = 0.1$ and $m > 1$, $e^{-2m}\tan^2(1/4\theta(1)) < 8\times10^{-5}$; thus, the term $e^{-2m}\tan^2(1/4\theta(1))$ in Eq. (A14) and the last term in Eq. (A15) can be safely neglected. In the limit of zero force $(m=0)$, expression (A14) predicts the correct value of $X_{cc}=2$. When the force is large $(m\to\infty)$, $X_{cc}\to 2(1+a/L)$. Comparison of the predictions of Eq. (A14) with the corresponding exact values [Eqs. (A1)–(A3)] suggests that Eq. (A14) is accurate within better than 0.5% when $a/L=0.1$ and $m>3$.

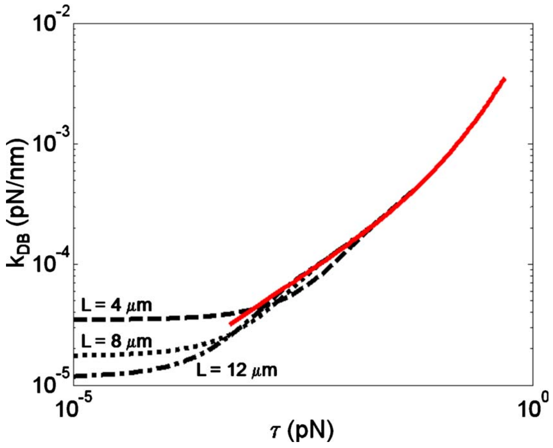

FIG. 15. (Color online) The system's spring constant k_{DB} (pN/nm) is depicted as a function of the force τ (pN). The dashed line, dotted line, and dash-dot line correspond respectively, to filaments with half length $L=4$, 8, and 12 μm. The solid (red) line corresponds to the asymptotic expression for large τ [Eq. (A17)].

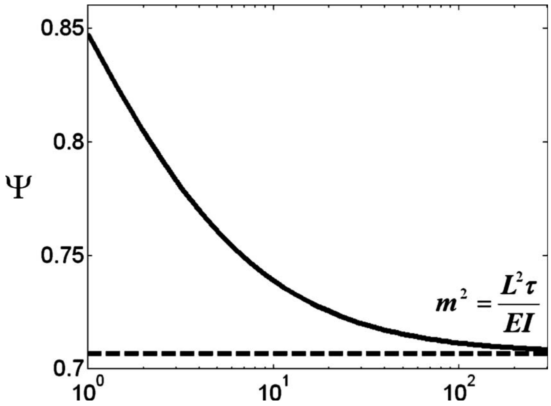

FIG. 16. Ψ as a function of $\hat{m}^2 = a^2\tau/EI$ (solid line). The dashed line depicts the large $\hat{m}^2$ asymptote.

When $m \gg 1$, Eq. (A15) can be simplified even further to yield

$$\varepsilon_\ell \sim \frac{a}{L} - \frac{1}{m}(2-\sqrt{2}) + \frac{1}{2\sqrt{2}m^3}\left(\frac{L}{a}\right)^2 - \frac{1}{2m^4}\left(\frac{L}{a}\right)^3 + O(m^{-5}). \tag{A16}$$

Figure 14 depicts the relative extension $\varepsilon_l = (X_{cc}-2)/2$ as a function of the dimensionless force $m^2 = \tau L^2/(EI)$ when $a/L=0.1$. The exact solution $(0<m<3)$ is depicted with a solid line with circles. The dashed line with the upward pointing triangles corresponds to the asymptotic solution Eq. (A15). The dotted line (inset only) corresponds to the small m asymptote Eq. (A7). The dashed-dot line (main figure only) corresponds to the approximation for very large m Eq. (A16). Witness that Eq. (A7) provides an excellent approximation when $m<1$, and Eq. (A15) works well when $m>1.5$.

4. Spring constant of the dumbbell

We define the dimensional spring constant of the dumbbell system as $k_{DB} = LdX_{cc}/d\tau = (2Ld\varepsilon/d\tau)^{-1}$ (N/m). Figure 15 depicts the spring constant k_{DB} (pN/nm) as a function of the force τ (pN) when $L=4$ μm (dashed line), 8 μm (dotted line), and 12 μm (dashed-dot line). The solid (red) line corresponds to the asymptotic expression for large τ [see Eq. (A17) below]. When the force is very small $(\tau\to0)$, $k_{DB}\sim EI/2a^2L$ is independent of τ and inversely proportional to L. As τ increases, the spring constants of the various systems approach rapidly the asymptotic value [Eq. (A17) below], which is independent of the filament's length. The length independence of the spring constant for relatively large values of τ is not surprising. At moderate and large forces, most of the filament is flat, and only small lengths, on the order of $m^{-1}L$ close to the beads participate in the deformation process.

To obtain an approximation for k_{DB} which is valid for moderate and large forces (i.e., $m^2>3$), we take the inverse of the derivative of the first term on the right hand side of Eq. (A15).

$$k_{DB} \sim \left(\frac{1}{1-\Psi}\right)\sqrt{\frac{\tau^3}{4EI}} \tag{A17}$$

where $\Psi = \frac{\hat{m}(1+\sqrt{1+2\hat{m}^2})}{[\sqrt{2}\sqrt{\hat{m}^2(2\hat{m}^2-1)+(2\hat{m}^2+1)^{3/2}-1}]}$ is independent of the filament's length L and $\hat{m}^2 = a^2\tau/EI = m^2(a/L)^2$. For example, when a-0.5 μm, $\tau=1$ pN, and $EI = 7\times10^{-26}$ Nm^2 (actin filament), $k_{DB} \sim 8.4\times10^{-3}$ pN/nm. Figure 16 depicts Ψ as a function of $\hat{m}^2 = a^2\tau/EI$. As $\hat{m}^2$ increases, Ψ approaches its asymptotic value of $2^{-1/2}$. In many circumstances, $\Psi \sim 0.7$ and $k_{DB} \sim 1.7\sqrt{\tau^3/EI}(1+1.8\hat{m}^{-2})$. When $\tau > 10EI/L_2$, the exact and asymptotic values of k_{DB} agree nearly perfectly. Witness that at large τ, $k_{DB} \sim \tau^{3/2}$.

---

[1] M. E. Arsenault, H. Zhao, P. K. Purohit, Y. E. Goldman, and H. H. Bau, Biophys. J. **93**, L42 (2007).

[2] M. E. Arsenault, Y. Sun, H. H. Bau, and Y. E. Goldman, Phys. Chem. Chem. Phys. **11**, 4834 (2009).

[3] T. Yanagida, M. Nakase, K. Nishiyama, and F. Oosawa, Nature (London) **307**, 58 (1984).

[4] F. Gittes, B. Mickey, J. Nettleton, and J. Howard, J. Cell Biol. **120**, 923 (1993).

[5] A. Ashkin, Phys. Rev. Lett. **24**, 156 (1970).

[6] A. Ashkin, J. M. Dziedzic, J. E. Bjorkholm, and S. Chu, Opt. Lett. **11**, 288 (1986).

[7] K. Svoboda and S. M. Block, Annu. Rev. Biophys. Biomol. Struct. **23**, 247 (1994).

[8] A. D. Mehta, J. T. Finer, and J. A. Spudich, Methods Enzymol. **298**, 436 (1998).

[9] A. D. Mehta, M. Rief, J. A. Spudich, D. A. Smith, and R. M. Simmons, Science **283**, 1689 (1999).

[10] Y. Tsuda, H. Yasutake, A. Ishijima, and T. Yanagida, Proc. Natl. Acad. Sci. U.S.A. **93**, 12937 (1996).

[11] S. B. Smith, Y. J. Cui, and C. Bustamante, Science **271**, 795 (1996).

[12] T. T. Perkins, S. R. Quake, D. E. Smith, and S. Chu, Science **264**, 822 (1994).

[13] D. E. Dupuis, W. H. Guilford, J. Wu, and D. M. Warshaw, J. Muscle Res. Cell Motil. **18**, 17 (1997).

[14] D. Riveline, C. H. Wiggins, R. E. Goldstein, and A. Ott, Phys. Rev. E **56**, R1330 (1997).

[15] S. B. Smith, Y. J. Cui, and C. Bustamante, Methods Enzymol. **361**, 134 (2003).

[16] M. D. Wang, H. Yin, R. Landick, J. Gelles, and S. M. Block, Biophys. J. **72**, 1335 (1997).

[17] S. B. Smith, L. Finzi, and C. Bustamante, Science **258**, 1122 (1992).

[18] B. Schnurr, F. Gittes, F. C. MacKintosh, and C. F. Schmidt, Macromolecules **30**, 7781 (1997).

[19] P. A. Janmey, S. Hvidt, J. Peetermans, J. Lamb, J. D. Ferry, and T. P. Stossel, Biochemistry **27**, 8218 (1988).

[20] http://www.dow.com/glycerine/resources/table18.htm Copyright © The Dow Chemical Company (1995–2010). All Rights Reserved.

[21] C. Veigel, M. L. Bartoo, D. C. S. White, J. C. Sparrow, and J. E. Molloy, Biophys. J. **75**, 1424 (1998).

[22] Y. Takagi, E. E. Homsher, Y. E. Goldman, and H. Shuman, Biophys. J. **90**, 1295 (2006).

[23] K. C. Neuman and S. M. Block, Rev. Sci. Instrum. **75**, 2787 (2004).

[24] See supplementary material at http://link.aps.org/supplemental/10.1103/PhysRevE.82.051923 for optical trap calibration details.

[25] L. D. Landau and E. M. Lifshitz, *Course in Theoretical Physics Vol. 7: Theory of Elasticity* (Pergamon, London, 1959).

[26] C. Brennen and H. Winet, Annu. Rev. Fluid Mech. **9**, 339 (1977).

[27] A. Bokaian, J. Sound Vib. **142**, 481 (1990).

[28] K. Towles, J. F. Beausang, H. G. Garcia, R. Phillips, and P. C. Nelson, Phys. Biol. **6**, 025001 (2009).

[29] M. E. Arsenault, Ph.D. thesis, University of Pennsylvania (2009).